NANO LETTERS

Letter

pubs.acs.org/NanoLett

PbS Nanocrystal Emission Is Governed by Multiple Emissive States

Justin R. Caram, Sophie N. Bertram, Hendrik Utzat, Whitney R. Hess, Jessica A. Carr, Thomas S. Bischof,[†] Andrew P. Beyler, Mark W. B. Wilson,[‡] and Moungi G. Bawendi*

Department of Chemistry, Massachusetts Institute of Technology, 77 Massachusetts Avenue, Cambridge, Massachusetts 02139, United States

Supporting Information

ABSTRACT: Lead chalcogenide colloidal nanocrystals (NCs) are promising materials for solution processable optoelectronics. However, there is little agreement on the identity and character of PbS NC emission for different degrees of quantum confinement—a critical parameter for realizing applications for these nanocrystals. In this work, we combine ensemble and single NC spectroscopies to interrogate preparations of lead sulfide NCs. We use solution photon correlation Fourier spectroscopy (S-PCFS) to measure the average single NC linewidth of near-infrared-emitting PbS quantum dots and find it to be dominated by homogeneous broadening. We further characterize PbS NCs using temperature-dependent linear and time-resolved emission spectroscopy which demonstrate that a kinetically accessed defect state dominates room temperature emission of highly confined emitting NCs. These experiments, taken together, demonstrate that the linewidth and Stokes shift of PbS NCs are the result of emission from two states: a thermally accessed defect—with an energetically pinned charge carrier—and an inhomogeneously broadened band-edge state.

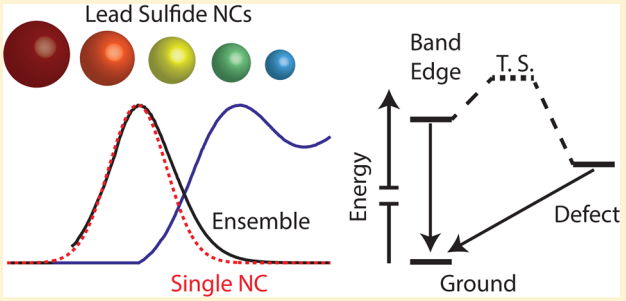

KEYWORDS: *Colloidal quantum dots, PbS nanocrystals, nanoparticle synthesis, photon correlation Fourier spectroscopy, semiconductor nanocrystals, spectral linewidth, near infrared emission*

Lead sulfide nanocrystals (NCs) can be synthesized with size-tunable bandgaps spanning the near and short-wavelength infrared (NIR 700−1000 nm and SWIR 1000−1600 nm) for applications beyond the bandgap of silicon—including photodetectors,[1] light-emitting diodes,[2] photovoltaics,[3] and incoherent up/downconversion of infrared light.[4,5] However, optimizing performance for these applications relies on understanding electronic properties of heterogeneous preparations of NCs. Significant recent effort has gone into improving the reproducibility and quality of PbS NC syntheses, including altering precursor reactivity,[6] precursor stoichiometry,[7] and understanding the role of hydroxyl anions for surface passivation.[8] In these experiments researchers use ensemble photoluminescence (PL) linewidth to report on size heterogeneity, trap density, and intrinsic electron phonon coupling—critical properties for applications.[9,10] However, estimates of the narrowest possible linewidth for PbS NCs diverge considerably. For example, for NIR-emitting PbS QDs, single NC studies show linewidths of <100 meV (by inspection),[11] while temperature-dependent ensemble size-selected photoluminescence excitation spectroscopy find homogeneous line-broadening in excess of 160 meV for similar samples.[12] In this study, we combine results from solution photon correlation Fourier spectroscopy (S-PCFS)—a method which measures the average single NC linewidth with temperature-dependent ensemble spectroscopy to disentangle PL line-broadening mechanisms for PbS QDs. Insight from these experiments allows us to propose a general model that explains the origin of PbS NC linewidths and provides a path for synthetic optimization.

Nanocrystal linewidths can be decomposed into intrinsic and ensemble contributions. The intrinsic linewidth is that measured from a single NC. This linewidth can arise from one or multiple emissive states, each homogeneously broadened through coupling to the local environment (for example electron−phonon coupling). The ensemble linewidth is the convolution of the intrinsic linewidth with a heterogeneous polydisperse ensemble. We present four experimental findings in this manuscript which we use to uncover the intrinsic emissive properties of PbS QDs. (1) We show that PbS NCs display increasing spectral linewidth and Stokes shift with decreasing size. (2) We find that these NCs display characteristic size-dependent line shape asymmetry which can be fit to two emissive states, one which shifts with respect to the first exciton peak and another that stays fixed. (3) We use S-PCFS to demonstrate that NIR emitting PbS NCs have broad intrinsic linewidths. (4) We use temperature-dependent linear and time-resolved emission measurements to show two interconverting states in small and intermediate sized NCs. We conclude that emission from individual PbS quantum dots arises from two states: a pinned-charge defect state and a

Received: May 27, 2016
Revised: September 8, 2016
Published: September 14, 2016

DOI: 10.1021/acs.nanolett.6b02147
Nano Lett. 2016, 16, 6070−6077

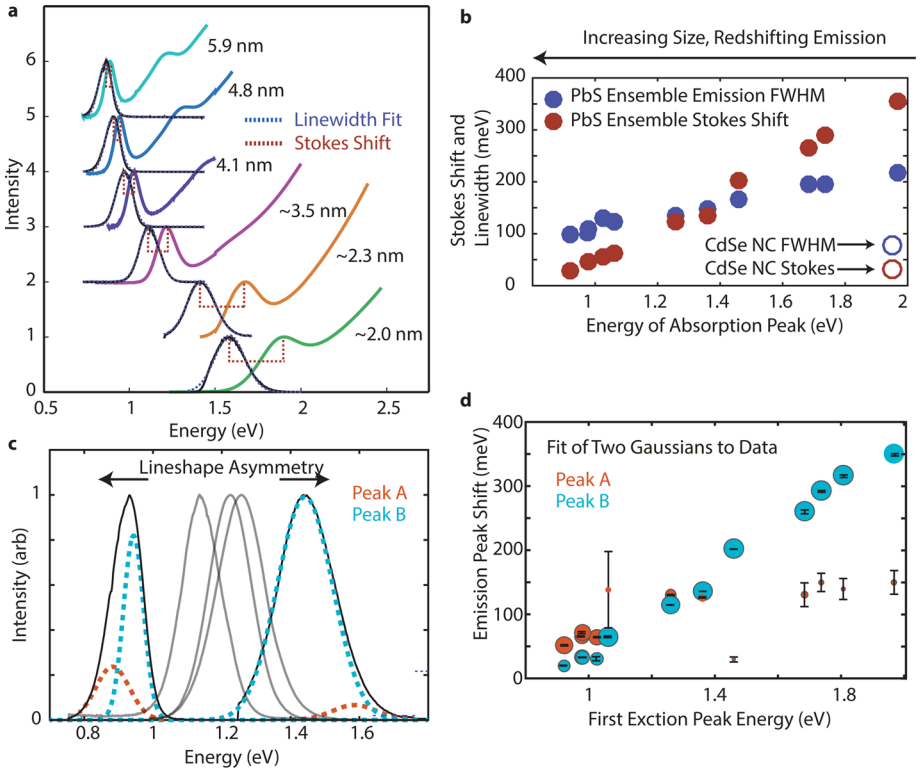

Figure 1. Size-dependent optical properties of PbS quantum dots. (a) Six representative absorption and emission spectra for different PbS NC preparations. We fit the photoluminescent linewidth to a single Gaussian function and find the Stokes shift relative to the first exciton absorption peak, plotting both in part (b) against their first exciton absorption energy. We observe monotonically increasing ensemble linewidths and Stokes shifts. A typical ensemble linewidth and Stokes shift of a CdSe NC preparation is shown for comparison (hollow circles). (c) Emission spectra of PbS QDs show a size-dependent asymmetric line shape, with small PbS PL spectra displaying an elongated tail to the blue and larger dots showing tails elongated to the red. (d) We fit this to two Gaussian functions (eq 1, labeled A and B, and plot their peak positions relative to the first exciton peak with orange and blue dots. The size of the dot reflects the magnitude of that Gaussian peak's contribution to the total fit of the PL spectrum. The error bars are the standard deviation of the peak position of each Gaussian, calculated from the square root of the diagonal of the covariance matrix calculated during least-squares fitting.

band-edge state. The contribution of each state to the overall emission depends on the size of the nanocrystal, which sets the energy of each state, and the temperature, which sets the rate of transition from band-edge to defect over an activation barrier. Our model reproduces the trends in size-dependent emission spectra and temperature-dependent lifetimes.

A key challenge for addressing the origin of PbS emission lineshapes is the large variation in ensemble spectral properties as a function of size. We illustrate the absorption and emission properties of a size series of PbS quantum dots in Figure 1a, synthesized according to refs 13 and 14. In contrast to CdSe quantum confined NCs, PbS nanoparticles manifest a highly size-dependent ensemble PL linewidth and Stokes shift.[15,16] Small, near IR (~2 nm 700–900 nm) emitting NCs display broad ensemble linewidths (160–240 meV) and large Stokes shifts (150–400 meV), while larger PbS NCs (emitting from 1200 to 1600 nm) have narrower PL linewidths (<100 meV) and smaller Stokes shifts (~30–80 meV), akin to their CdSe NC counterparts (Figure 1b).[17] Size polydispersity naturally leads to inhomogeneous line broadening and higher apparent Stokes shift due to the increased absorption of a higher volume subensemble consistent with inhomogeneous line broadening.[18] Transmission electron microscopy (TEM) shows greater morphological polydispersity in smaller PbS quantum dots, however photoluminescent excitation spectroscopy (Figure S1a–c, and shown elsewhere[12]) suggest size heterogeneity is not the dominant contribution to the observed ensemble linewidth for small PbS quantum dots.

We reproduce the analysis done in ref 16 and find that the emission spectra of an ensemble of PbS QDs show a distinct asymmetry (Figure 1c–d).We find that this asymmetry is best characterized as emission arising from two distinct features, which we label A and B, respectively. In Figure 1c, we fit the observed emission spectrum to two Gaussians

$$\mathrm{PL}(E) = C_{\mathrm{A}} e^{-(E-E_{\mathrm{A}})^2/2\sigma_{\mathrm{A}}^2} + C_{\mathrm{B}} e^{-(E-E_{\mathrm{B}})^2/2\sigma_{\mathrm{B}}^2} \quad (1)$$

where the average energy and standard deviation of the first and second features are $E_{\mathrm{A,B}}$ and $\sigma_{\mathrm{A,B}}$ respectively. We find that E_{A} stays fixed while E_{B} shifts when both energies are compared to the first absorption feature as a function of size. This shift gives rise to the observed change in direction of the PL asymmetry in the PL feature from small to large NCs.

To assess the intrinsic linewidth of NIR emitting PbS QDs we perform S-PCFS on NCs that emit below 950 nm (the spectral window of silicon single photon counting modules). S-PCFS has been described elsewhere[19−21] and has been used to study average single molecule linewidths of CdSe/CdS, InP, and InAs quantum dots. We rederive the main spectroscopic result in the Supporting Information. S-PCFS allows us to reliably extract the *average* single-molecule linewidths from an ensemble of quantum dots in solution. As Figure 2a displays, NCs diffuse through the focus of a confocal microscope

DOI: 10.1021/acs.nanolett.6b02147
Nano Lett. 2016, 16, 6070−6077

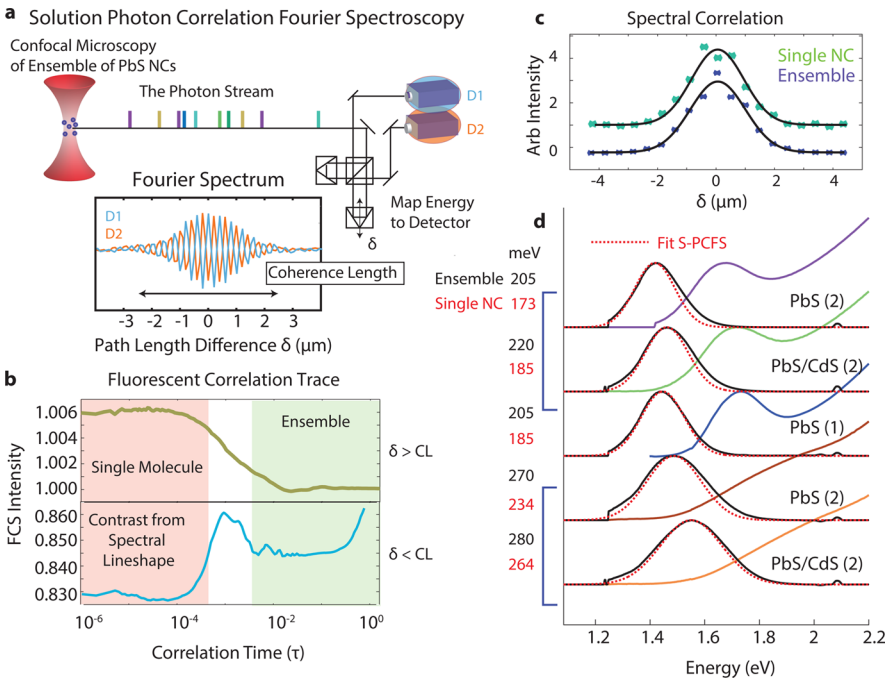

Figure 2. (a) Solution photon correlation Fourier spectroscopy (S-PCFS) schematic. The photon stream is directed through a Michelson interferometer with varying path length to single photon avalanche photodiodes which allow us to time the photon arrivals. The overall intensity is modulated at each detector according to the path length difference, δ, and the coherence length (CL) of the emission, demonstrated with the plotted Fourier spectrum of the inset. (b) The detector cross-correlation beyond and within the CL of quantum dot emission. We observe a fluorescence correlation trace at $\delta >$ CL and spectrally induced modulation at $|\delta| <$ CL. (c) Typical ensemble and single NC spectral correlations. We fit this using Supporting Information eq 24 to generate single molecule spectra plotted against the ensemble PL spectra in (d). On the left, typical single molecule and ensemble spectral linewidths. The groupings represent the same core with and without an exchanged cadmium shell. We observe little difference between ensemble and single molecule linewidths in all cases. Samples labeled 1 (2) were prepared using lead acetate (lead oxide) as a precursor.

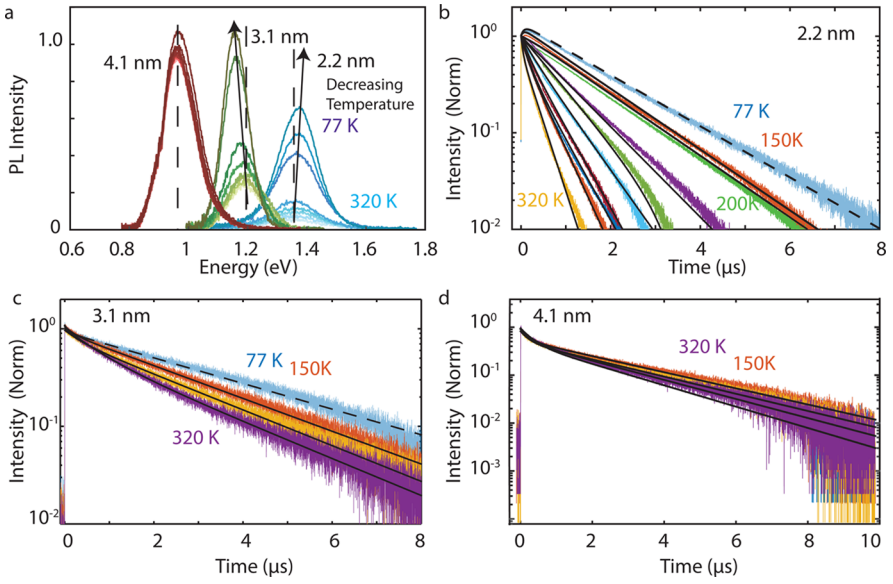

Figure 3. (a) Temperature-dependent emission spectra for 2.2, 3.1, and 4.1 nm PbS quantum dots (900, 1050, and 1300 nm emission), with time-resolved PL spectra plotted in b–d for each ensemble, respectively. In 2.2 nm QDs we observe a slight early time rise, which we attribute to higher quantum efficiency of the InGaAs detector for red-shifted QD emission. In (b) we plot time-resolved PL for 77, 150, and 200–320 K in steps of 20 K. In (c–d) we plot 77, 220, 260, and 320 K time-resolved emission. All fits are to eq 2 and plotted as a solid line. We dim the 77 K data and plot the two-exponential fit with a dashed line to denote its qualitatively different behavior.

generating a photon stream which passes through a variable arm Michelson interferometer. We measure the second-order correlation function, which at short time differences (τ) is enriched with single molecule contrast, akin to fluorescence correlation spectroscopy. We move one arm of the interferometer through equal path lengths with 500 nm steps and at each step oscillate the stage over the central energy of emission (~900 nm). This oscillation induces an anticorrelated signal, which is the PCFS interferogram, that includes both the ensemble and the *average* single NC spectral correlation (the

DOI: 10.1021/acs.nanolett.6b02147
Nano Lett. 2016, 16, 6070–6077

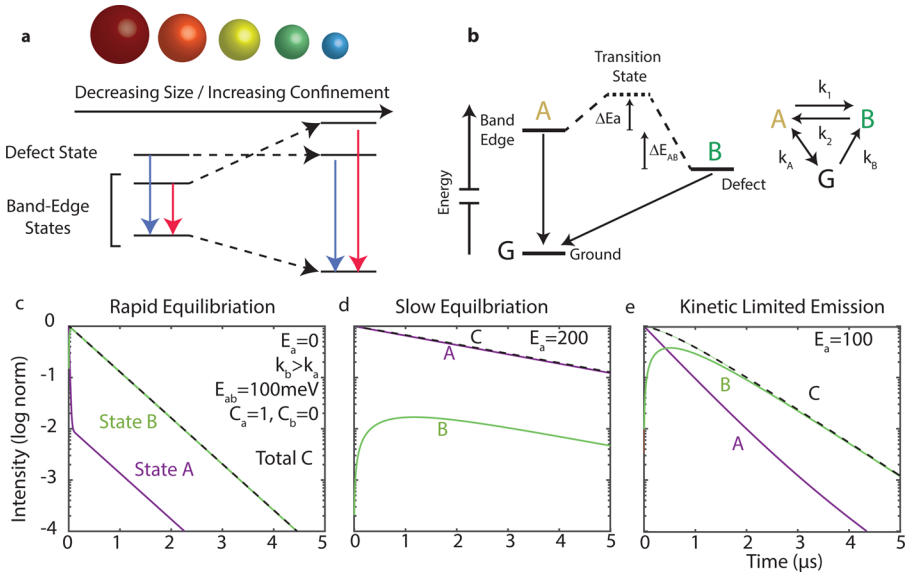

Figure 4. (a) PbS QDs emit from band-edge or pinned-energy defect states depending on NC size. Larger dots have lower energy band-edge emission, while smaller dots have lower energy defect emission. (b) We model time-resolved emission, by invoking two states, A and B, that can interchange over a transition state barrier according to temperature-dependent rate constants k_1 and k_2. They can also relax to the ground state via independent rate constants k_A and k_B. (c−e) We plot the time-resolved populations of the band-edge state (purple/A), defect state, (green/B), and total excited state (black dashed line C) for 0 (c), 200 (d), and 100 (e) meV activation barriers. We use the parameters provided in figure (c) applied to Supporting Information eqs 31−33 to determine the population of each state based on the model described above.

autocorrelation of the fluorescence spectrum, Figure 2b). After processing, we fit the average single NC PCFS interferogram (Figure 2c) to the Fourier transform of the autocorrelation of a two-component Gaussian spectrum (described further in the Supporting Information) to extract the average single molecule linewidth for different preparations of PbS nanocrystals. In Figure 2d, we plot the intrinsic linewidth of three different preparations of PbS NCs; one prepared using lead acetate as a precursor labeled (1) and two prepared using lead oxide as a precursor (2), the latter also grown with a thin shell of CdS. For all five samples the average single NC linewidth closely matches the ensemble linewidth, suggesting that the majority of line broadening is intrinsic to the nanocrystal. The center spectrum is only plotted below 1.4 eV due to incomplete solvent background subtraction.

We study the temperature dependence of PbS NC emission to probe whether the two states suggested in Figure 1 *interconvert*, resulting in the observed linewidth. In Figure 3a we show temperature-dependent PL emission of three dilute samples with first absorption features at 700, 950, and 1200 nm, respectively, all prepared using method (1). We observe large temperature-dependent variation for two of the samples, consistent with prior measurements.[22,23] We plot the emission spectra of each sample as we vary the temperature from 77 to 320 K. In the Supporting Information we show that each spectra fits well to eq 1, reproducing the observed blue and red-shifting by changing the width and intensity of each feature. Furthermore, we find that PbS QD quantum yield also increases with decreased temperature, correlated to longer PL lifetimes plotted in Figure 3b−d. We fit the time-resolved photoluminescence to two exponentials,

$$C(t) = C_+ e^{-r_{(+)}t} + C_- e^{-r_{(-)}t} \quad (2)$$

where + and − refer to "slow" and "fast" rates, respectively. These two rates demonstrate the presence of at least *two states* with different lifetimes contributing to the overall PL. The ability to modulate the relative contribution of each state using temperature strongly suggests that these states can interconvert during the microsecond emission lifetime of PbS QDs. In Supporting Figure S3, we examine spectrally resolved emission of 3.1 nm QDs observing spectrally dependent biexponential behavior consistent with transfer from between states.

In Figure 4 we combine the information in Figures 1−3 to construct a model that reproduces the observation of broad NIR linewidths and temperature-dependent biexponential rates in PbS quantum dots. As Figure 1d shows, the size-dependent ensemble emission spectra are best described by two Gaussian functions: one whose average energy stays constant relative to the band-edge absorption feature (A), and one which shifts linearly (B). The behavior of state A's peak energy is consistent with emission from two size-confined carriers. In turn, the energetic shift of state B relative to the first-exciton peak reflects emission from at least one carrier in a nonsize dependent (pinned) conduction and/or valence band. Transitions arising from defect/pinned carriers and confined electrons or holes are invoked to explain the large Stokes shift, broad linewidths, and weak size tunability of the emission from ternary QDs, such as $CuInS_2/Se_2$[24,25] and Cu^+ doped CdSe NCs.[26] Furthermore, sub-band gap defect states in PbS NCs have been suggested by both experiment and theory, with varying explanations including partial oxidation, nonstoichiometry, incomplete surface passivation, and shape anisotropy.[10,23,27−31] Therefore, in Figure 4a we assign peak A to band-edge recombination and peak B to recombination of a confined carrier with a pinned defect, for simplicity drawn as the electron. The relative positions of defect and band-edge change as a function of NC diameter. In small PbS NCs, the defect emission sits below the band edge, while in larger NCs the defect is above the band edge. This results in blue-shifted or red-shifted asymmetric lineshapes for small and large dots, respectively.

In Figure 2 we use S-PCFS to demonstrate that NIR emitting PbS QD emission is intrinsically broad despite morphological

DOI: 10.1021/acs.nanolett.6b02147
Nano Lett. 2016, 16, 6070−6077

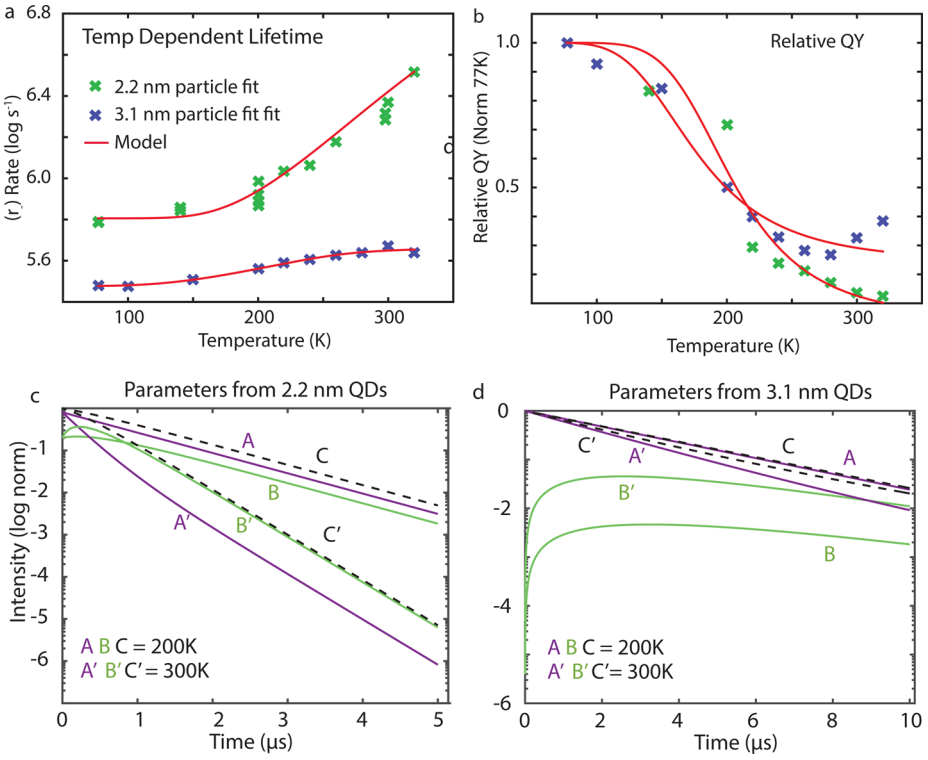

Figure 5. (a) The temperature-dependent rate constant from Figure 3c–d fit to the model proposed in Figure 4b (using Supporting eq 35). (b) The integrated relative quantum yield (relative to 77 K) from the data shown in Figure 3a, fit to supplemental eq 38. (c–d) Band-edge, (A) defect (B), and total (C) emission at 200 and 300 K (X and X′, respectively) using averaged parameters from Table 1 applied to Supporting Information eqs 31–33 for 2.2 nm QDs (c) and 3.1 nm (d).

polydispersity (as shown in Supporting Figure S1a–c). This provides direct evidence of defect emission for small PbS QDs. Defect states typically show large homogeneous linewidths due to higher NC polarizability leading to increased electron–phonon coupling.[32] Prior studies of NIR PbS QDs have suggested that the observed broad linewidths are a result of various mechanisms including hybrid state emission,[30] defect emission,[16] complex fine structure,[31] and strain induced acoustic phonon coupling.[12] Our results point to intrinsically broad emission due to polarizability induced coupling to phonon modes.

Completing the model, we study what mediates band-edge to defect (and back) transitions in PbS QDs. The presence of two features in the emission spectrum and two decay rates whose relative contributions are modulated by temperature leads us to employ a kinetic model illustrated in Figure 4b. Critically, we find that four rates govern the emissive properties of PbS NCs from 150 to 320 K:

$$\mathrm{A} \underset{k_2}{\overset{k_1}{\rightleftharpoons}} \mathrm{B}, \quad \mathrm{A} \xrightarrow{k_A} \mathrm{G}, \quad \mathrm{B} \xrightarrow{k_B} \mathrm{G} \tag{3}$$

$$k_1 = A_p e^{-\beta(E_a)}, \quad k_2 = A_p e^{-\beta(E_a + \Delta E_{AB})} \tag{4}$$

where $k_{A,B}$ and $k_{1,2}$ represent decay to the ground state and transport between each state over an activation barrier, respectively. k_1 and k_2 are determined by several parameters: the energy difference between defect and band-edge states E_{AB}, an activation energy E_a, $\beta = (k_{boltz}T)^{-1}$, and an attempt frequency A_p. We solve this rate equation in the Supporting Information and Figure 4c–d shows several qualitative features this model. Starting with an excited state population in State A ($C_A = 1$, $C_B = 0$), faster emission rates from the defect than the band edge ($k_B > k_A$) and a large energy difference between states A and B ($E_{AB} = 100$ meV) we vary the activation barrier (E_a) from 0 to 200 meV to understand how transfer effects time-resolved photoluminescence at room temperature. We plot the population states A, B, and the total excited state population. For no activation barrier (Figure 4c), the populations quickly equilibrate and the NCs decay primarily from state B. In Figure 4d the activation barrier is not overcome at room temperature, leading to emission from state A. In Figure 4e, transfer between states over the activation barrier competes with emission, leading to PL from State A initially, followed by emission from state B. The total decay is biexponential, in agreement with our observations in Figure 3b–d.

This model reproduces several qualitative features of the emission of PbS QDs. For the smallest dots studied, we observe blueshifting emission with decreasing temperature, consistent with an initially populated band-edge state that is at a higher energy than the defect state. If the band-edge state has a higher quantum yield than the defect state, we anticipate increasing emission intensity with decreasing temperature, also observed for small and intermediate QDs. Furthermore, in 2.2 nm QDs, the band edge can provide a long-lived reservoir for defect emission at lower temperatures, resulting in detection of delayed emission (observed in Figure 3b). We define delayed emission as slowed dynamics at early times (e.g., when one prefactor, $C_{\pm}$, is negative), resulting in the phenomenological bending of the PL curve. Figure 3b exaggerates this effect due the increased sensitivity of InGaAs avalanche photodiodes above 950 nm, leading to preferential detection of red-shifted defect emission. In larger QDs (Figure 3c–d), the defect

DOI: 10.1021/acs.nanolett.6b02147
Nano Lett. 2016, 16, 6070–6077

Table 1. Parameters Obtained from Fitting Equations 35 ($r_{(-)}$) and 36 (QY) from the Supporting Information to the Data Presented Figure 5a–b[a]

fit parameter	E_a (meV)	E_{AB} (meV)	k_A (s^{-1})	k_B (s^{-1})	A_p (s^{-1})	C_A	C_B
$r^{(-)}_{2.2nm}$	110	100	5.3×10^5	2.5×10^6	1.3×10^8		
$QY_{2.2nm}$	120	60	6.0×10^5	3.0×10^6	1.6×10^8	0.8	0.2
$r^{(-)}_{3.1nm}$	130	−90	2.0×10^5	3.1×10^5	0.5×10^7		
$QY_{3.1nm}$	100	−60	3.0×10^5	4.0×10^5	1.0×10^7	1.0	0

[a]Subscripts represent the average size of nanocrystal studied.

energy sits higher than the band edge resulting in increased band-edge character in the emission across all temperatures when compared to the smaller QDs. For the largest dots, the defect sits high enough in energy that most of the emission arises from the band edge, which explains the relatively low Stokes shift and narrow linewidths observed. As a further test, in Figure S4 we plot emission energy resolved PL decay for 3.1 nm QDs, observing longer lifetimes for red-shifted emission, reflecting the changing defect/band-edge character across the emissive band.

In Figure 5a–b we fit two temperature-dependent experimental parameters to the model proposed in Figure 4b: the "slow" rate $r_{(-)}$ (Figure 5a), and the relative quantum yield (Figure 5b). We extract $r_{(-)}$ from exponential fits to the data plotted in b–d and fit it to equation S35. The relative QY is found by comparing the integrated intensity at each temperature to the 77 K spectrum and fit to equation S38 (assuming radiative and nonradiative rates are temperature-independent). All fit equations are derived in the Supporting Information. We report the fit parameters in Table 1 for each measurement. For small dots (2.2 nm), we find that we start with a large initial population in the band-edge state ($C_A = 0.8$) which has a longer lifetime than the defect state ($k_A = 5.6 \times 10^5$ s^{-1} and $k_B = 2.7 \times 10^6$ s^{-1}). The band-edge interconverts over a ∼ 115 meV (E_a) barrier to the defect state, which sits below the band-edge by 80 meV (E_{AB}), similar to the estimate from the fit to two Gaussian functions in Figure 1d (∼120 meV). Interestingly, in Figure 3b we continue to observe state interconversion at 77 K despite low transfer rates (∼10 s^{-1}) from our model. This suggests other states, invoked in prior models of PbS and PbSe emission below 150 K,[27,33] may contribute to the dynamics at low temperatures. Temperature effects are less pronounced for intermediate and large NCs, as the defect state sits higher in energy (∼75 meV) than the band edge, allowing for dominant band-edge recombination even during equilibration. In Figure 5c–d we plot the population of the band edge state (A), defect state (B), and total emission for 200 and 300 K. We observe qualitatively similar time-resolved photoluminescence to that plotted in Figure 3b–c. Figure 5c shows that the model predicts a large temperature-dependent change in 2.2 nm NC lifetimes, due to increased defect character in the emission at room temperature. Figure 5d illustrate that for 3.1 nm dots, the defect state only modulates the tail of the emission, similar to the observation of Figure 3c. To further confirm our model, in the Supporting Information we apply averaged fit constants to estimate the contribution of the band-edge state to the total emission, obtaining good agreement to experiment (figure S3).

In summary, two states govern the properties of PbS NC emission, a band-edge state and a defect state. The relative contribution of each state to the emissive properties of PbS QDs (Stokes shift, linewidth, lifetime) is governed by NC size and temperature. The defect state dominates emission at room temperature for NIR emitting PbS nanocrystals leading to broad homogeneous linewidths. Larger PbS NCs display more band-edge emission. The presence of a energetic barrier between band-edge and defect prevents rapid thermalization and complicates the assignment of low temperature fine structure. Upon cooling the competition of rates allows for more band-edge emission, for which size and shape inhomogeneity plays a larger role in governing the line shape. One distinct feature of PbS defect emission is its shorter lifetime compared to band-edge emission. Typically, weak overlap between localized electron and delocalized hole will increase the lifetime of the defect state. However, in PbS QDs, the increase in lifetime is masked by a decrease in quantum yield, which arises from more nonradiative pathways from the defect state. Accounting from the nearly 5-fold increase in quantum yield from defect to band-edge, the radiative rates are nearly identical.

Understanding the nature of the emissive state is of critical importance to extracting excitation and charge from Pb chalcogenide NC systems. However, assigning states in PbS nanocrystals remains a significant challenge. Due to a filled lead 6s orbital, PbS acts as an L-point semiconductor with a 64-fold band-edge degeneracy.[34,35] Further complicating the structure, a small optical band gap leads to significant perturbation from valence-conduction band mixing, spin–orbit coupling, and intervalley scattering. It is likely that similar to CdSe NCs, PbS emission is in part mediated by complex fine-structure, which complicates simple assignment to a band-edge and defect states.[36] Nevertheless, this qualitative model reproduces the data both numerically and phenomenologically. The presence of a homogeneously broadened defect state may partially account for anomalously fast triplet transport from NCs to organic materials[4] and high electron conductivity in NC films[1,37] due to broadened intrinsic linewidths which can increase charge and exciton transport. Furthermore, our results suggest that improving synthetic control over PbS NC size polydispersity may *not* be as critical as controlling or mitigating defect emission. Ternary NCs have shown that, by varying stoichiometry, defect emission can be suppressed in favor of band-edge emission.[25] A similar approach may improve PbS NCs for applications.

Methods. Samples labeled (1) were prepared using methods described in refs 13 and 14. The lead precursor is prepared by mixing lead (II) acetate trihydrate (99.999% trace metals basis, Aldrich), octadecene (ODE, 90%) (99%, Aldrich), and oleic acid (85%, TCI) in a three-neck flask stirred and degassed at room temperature for 30 min by pulling vacuum on the Schlenk line, then degassed at 120 °C for an hour until clear and colorless. The flask is placed under nitrogen and cooled to the injection temperature. The sulfur precursor was prepared from 10 mL of ODE and 213 μL of $(TMS)_2S$ (Aldrich, synthesis grade) in a nitrogen-filled glovebox. The sulfur solution is injected into the lead precursor when the solution reaches a set temperature (50–150) °C depending on the size

DOI: 10.1021/acs.nanolett.6b02147
Nano Lett. 2016, 16, 6070–6077

desired. For the smallest PbS particles samples the lead precursor was prepared using 2.00 mmol of lead acetate, mixed with 62.5 mmol of ODE and 4.436 mmol of OA. The injection was done at 50 °C. An ice bath was quickly used after injection to quench the reaction for 10 min. PbS core and PbS/CdS core/shell QDs (labeled 2) were prepared following a modified protocol by Liu et al.[38] Here the Pb-precursor consisted of PbO (0.900 g, 4.03 mmol 99.999%), OA (2.5 mL; 7.9 mmol), and ODE (37.5 mL) added to a 100 mL three-neck flask. The solution was degassed as before. The same procedure was followed for the S-precursor with 20 mL of degassed ODE under nitrogen were mixed with $(TMS)_2S$ (0.42 mL, 1.99 mmol). For each reaction, the molar ratio of Pb:S:OA was kept constant at approximately 2:1:4. Ten milliliters of Pb-precursor stock solution was heated to 30 °C under nitrogen. Five milliliters of S-precursor was subsequently injected into the flask, and the solution was heated to either 40 or 50 °C at a rate of 2 °C/min. PbS QD growth solutions were transferred to a glovebox for cation exchange and purification. The Cd precursor consisted of CdO (0.218 g, 1.70 mmol 99.99%), OA (1.6 mL, 5.1 mmol), and ODE (12.7 mL) added to a 50 mL three-neck flask. The solution was degassed at room temperature, heated to 200 °C under nitrogen until dissolved, and finally cooled to 100 °C for further degassing. For cation exchange, 0.3 mL of Cd precursor was added to 5 mL of the growth solution and stirred at room temperature for 5 min. PbS and PbS/CdS QDs were purified in the glovebox by precipitation with isopropanol, methanol, and butanol depending on the size. All sizes are determined from the first-exciton absorption peak using ref 39.

Solution-photon correlation Fourier spectroscopy was performed using a home-built interfereometer as described previously.[21] The emission stream from a dilute solution (~1000 emissive NCs) is collected through a confocal microscope and directed through a Michelson Interferometer with a 50/50 beam splitter. The variable path length is set by a ANT-130 linear encoded stage (Aerotech). The stage is stepped every 500 nm and oscillated at the central carrier energy of the emission. The emission is directed to two single photon counting modules (PerkinElmer SPCMs), and photon arrival times are recorded using a HydraHarp (PicoQuant) in T2 mode. We use home-built software to correlate each channel and analyze the sum and cross correlation signal as described in the Supporting Information.

For ensemble temperature-dependent emission measurements three preparations of PbS NCs (synthesized method 1 described above) were diluted in a solution of 4% poly(methylmethacrylate) by weight in toluene. The samples were then drop cast onto quartz substrates (ESCO Optics) and placed into a coldfinger cryostat (Janis). The cryostat was then evacuated and cooled to 77 K with liquid nitrogen. The coldfinger was heated and held at multiple temperatures from 77 to 320 K. The NC film was excited with at 532 nm, and the emission spectra were recorded on either an InGaAs photoidode (Thorlabs) using lock-in detection and a scanning monochromator. The same films were used to collect PL lifetimes and were excited using a pulsed diode laser (PicoQuant) at 532 nm, 100 kHz repetition rate. The emission from the NCs was directed to an InGaAs single photon counting module (Micro Photon Devices) connected to a time-correlated single photon counting card (PicoHarp 300, PicoQuant). Lifetimes were taken at each temperature, and repeated for over several days. All analysis was performed in Mathematica or Matlab.

■ ASSOCIATED CONTENT

Supporting Information

The Supporting Information is available free of charge on the ACS Publications website at DOI: 10.1021/acs.nanolett.6b02147.

Photoluminescent excitation spectra and TEM of NIR emitting PbS NCs, derivations of S-PCFS, and kinetic model used to fit temperature-dependent rates and quantum yields (PDF)

■ AUTHOR INFORMATION

Corresponding Author

*E-mail: mgb@mit.edu.

Present Addresses

†T.S.B.: 67 Cyclotron Rd, The Molecular Foundry, Lawrence Berkeley National Laboratory, Berkeley, CA 94720.

‡M.W.B.W.: 80 St. George Street, Rm. 241A, Toronto, Ontario, M5S 3H6, Canada.

Notes

The authors declare no competing financial interest.

■ ACKNOWLEDGMENTS

This work was primarily funded in part by the DOE Office of Science, Basic Energy Sciences, under Award No. DE-FG02-07ER46454. S.N.B., T.S.B., and M.W.B.W. were supported by the Department of Energy (DOE) through the DOE Center for Excitonics (an Energy Frontiers Research Center funded by the US DOE, Office of Science, Office of Basic Energy Sciences through Grant DE-SC0001088). J.A.C. and W.R.H. had Government support under and awarded by DoD, Air Force Office of Scientific Research, National Defense Science and Engineering Graduate (NDSEG) Fellowship, 32 CFR 168a.

■ REFERENCES

(1) Sargent, E. H. *Nat. Photonics* **2009**, *3*, 325−331.

(2) Supran, G. J.; Song, K. W.; Hwang, G. W.; Correa, R. E.; Scherer, J.; Dauler, E. A.; Shirasaki, Y.; Bawendi, M. G.; Bulovic, V. *Adv. Mater.* **2015**, *27*, 1437−1442.

(3) Tang, J.; Kemp, K. W.; Hoogland, S.; Jeong, K. S.; Liu, H.; Levina, L.; Furukawa, M.; Wang, X.; Debnath, R.; Cha, D.; Chou, K. W.; Fischer, A.; Amassian, A.; Asbury, J. B.; Sargent, E. H. *Nat. Mater.* **2011**, *10*, 765−771.

(4) Thompson, N. J.; Wilson, M. W. B.; Congreve, D. N.; Brown, P. R.; Scherer, J. M.; Bischof, T. S.; Wu, M.; Geva, N.; Welborn, M.; Voorhis, T. V.; Bulović, V.; Bawendi, M. G.; Baldo, M. A. *Nat. Mater.* **2014**, *13*, 1039−1043.

(5) Wu, M.; Congreve, D. N.; Wilson, M. W. B.; Jean, J.; Geva, N.; Welborn, M.; Van Voorhis, T.; Bulović, V.; Bawendi, M. G.; Baldo, M. A. *Nat. Photonics* **2015**, *10*, 31−34.

(6) Hendricks, M. P.; Campos, M. P.; Cleveland, G. T.; Jen-La Plante, I.; Owen, J. S. *Science* **2015**, *348*, 1226−1230.

(7) Weidman, M. C.; Beck, M. E.; Hoffman, R. S.; Prins, F.; Tisdale, W. A. *ACS Nano* **2014**, *8*, 6363−6371.

(8) Zherebetskyy, D.; Scheele, M.; Zhang, Y.; Bronstein, N.; Thompson, C.; Britt, D.; Salmeron, M.; Alivisatos, P.; Wang, L.-W. *Science* **2014**, *344*, 1380−1384.

(9) Zhitomirsky, D.; Kramer, I. J.; Labelle, A. J.; Fischer, A.; Debnath, R.; Pan, J.; Bakr, O. M.; Sargent, E. H. *Nano Lett.* **2012**, *12*, 1007−1012.

DOI: 10.1021/acs.nanolett.6b02147
Nano Lett. 2016, 16, 6070−6077

(10) Hwang, G. W.; Kim, D.; Cordero, J. M.; Wilson, M. W. B.; Chuang, C.-H. M.; Grossman, J. C.; Bawendi, M. G. *Adv. Mater.* **2015**, *27*, 4481−4486.
(11) Peterson, J. J.; Krauss, T. D. *Nano Lett.* **2006**, *6*, 510−514.
(12) Fernée, M. J.; Jensen, P.; Rubinsztein-Dunlop, H. *J. Phys. Chem. C* **2007**, *111*, 4984−4989.
(13) Hines, M. A.; Scholes, G. D. *Adv. Mater.* **2003**, *15*, 1844−1849.
(14) Zhao, N.; Osedach, T. P.; Chang, L.-Y.; Geyer, S. M.; Wanger, D.; Binda, M. T.; Arango, A. C.; Bawendi, M. G.; Bulovic, V. *ACS Nano* **2010**, *4*, 3743−3752.
(15) Cui, J.; Beyler, A. P.; Coropceanu, I.; Cleary, L.; Avila, T. R.; Chen, Y.; Cordero, J. M.; Heathcote, S. L.; Harris, D. K.; Chen, O.; Cao, J.; Bawendi, M. G. *Nano Lett.* **2016**, *16*, 289−296.
(16) Ushakova, E. V.; Litvin, A. P.; Parfenov, P. S.; Fedorov, A. V.; Artemyev, M.; Prudnikau, A. V.; Rukhlenko, I. D.; Baranov, A. V. *ACS Nano* **2012**, *6*, 8913−8921.
(17) Murray, C. B.; Norris, D.; Bawendi, M. G. *J. Am. Chem. Soc.* **1993**, *115*, 8706−8715.
(18) Liptay, T. J.; Marshall, L. F.; Rao, P. S.; Ram, R. J.; Bawendi, M. G. *Phys. Rev. B: Condens. Matter Mater. Phys.* **2007**, *76*, 155314.
(19) Brokmann, X.; Marshall, L. F.; Bawendi, M. G. *Opt. Express* **2009**, *17*, 4509−4517.
(20) Marshall, L. F.; Cui, J.; Brokmann, X.; Bawendi, M. G. *Phys. Rev. Lett.* **2010**, *105*, 053005.
(21) Cui, J.; Beyler, A. P.; Marshall, L. F.; Chen, O.; Harris, D. K.; Wanger, D. D.; Brokmann, X.; Bawendi, M. G. *Nat. Chem.* **2013**, *5*, 602−606.
(22) Turyanska, L.; Patanè, A.; Henini, M.; Hennequin, B.; Thomas, N. R. *Appl. Phys. Lett.* **2007**, *90*, 101913−101914.
(23) Gaponenko, M. S.; Lutich, A. A.; Tolstik, N. A.; Onushchenko, A. A.; Malyarevich, A. M.; Petrov, E. P.; Yumashev, K. V. *Phys. Rev. B: Condens. Matter Mater. Phys.* **2010**, *82*, 125320.
(24) Nose, K.; Omata, T.; Otsuka-Yao-Matsuo, S. *J. Phys. Chem. C* **2009**, *113*, 3455−3460.
(25) Jara, D. H.; Stamplecoskie, K. G.; Kamat, P. V. *J. Phys. Chem. Lett.* **2016**, *7*, 1452−1459.
(26) Whitham, P. J.; Knowles, K. E.; Reid, P. J.; Gamelin, D. R. *Nano Lett.* **2015**, *15*, 4045−4051.
(27) Gao, J.; Johnson, J. C. *ACS Nano* **2012**, *6*, 3292−3303.
(28) De Geyter, B.; Houtepen, A. J.; Carrillo, S.; Geiregat, P.; Gao, Y.; ten Cate, S.; Schins, J. M.; Van Thourhout, D.; Delerue, C.; Siebbeles, L. D. A.; Hens, Z. *ACS Nano* **2012**, *6*, 6067−6074.
(29) Zhang, J.; Jiang, X. *J. Phys. Chem. B* **2008**, *112*, 9557−9560.
(30) Rubinsztein-Dunlop, M. J. F.; Thomsen, E.; Jensen, P.; Halina. *Nanotechnology* **2006**, *17*, 956−957.
(31) de Lamaëstre, R.; Bernas, H.; Pacifici, D.; Franzó, G.; Priolo, F. *Appl. Phys. Lett.* **2006**, *88*, 181115−181116.
(32) Fröhlich, H. *Adv. Phys.* **1954**, *3*, 325−361.
(33) Grodzińska, D.; Evers, W. H.; Dorland, R.; van Rijssel, J.; van Huis, M. A.; Meijerink, A.; de Mello Donegá, C.; Vanmaekelbergh, D. *Small* **2011**, *7*, 3493−3501.
(34) Kang, I.; Wise, F. W. *J. Opt. Soc. Am. B* **1997**, *14*, 1632−1646.
(35) Olkhovets, A.; Hsu, R.-C.; Lipovskii, A.; Wise, F. W. *Phys. Rev. Lett.* **1998**, *81*, 3539−3542.
(36) Norris, D. J.; Efros, a. L.; Rosen, M.; Bawendi, M. G. *Phys. Rev. B: Condens. Matter Mater. Phys.* **1996**, *53*, 16347−16354.
(37) Lee, J.-S.; Kovalenko, M. V.; Huang, J.; Chung, D. S.; Talapin, D. V. *Nat. Nanotechnol.* **2011**, *6*, 348−352.
(38) Liu, T.-Y.; Li, M.; Ouyang, J.; Zaman, M. B.; Wang, R.; Wu, X.; Yeh, C.-S.; Lin, Q.; Yang, B.; Yu, K. *J. Phys. Chem. C* **2009**, *113*, 2301−2308.
(39) Moreels, I.; Lambert, K.; Smeets, D.; De Muynck, D.; Nollet, T.; Martins, J. C.; Vanhaecke, F.; Vantomme, A.; Delerue, C.; Allan, G.; Hens, Z. *ACS Nano* **2009**, *3*, 3023−3030.

DOI: 10.1021/acs.nanolett.6b02147
Nano Lett. 2016, 16, 6070−6077